

Design and analysis of a SF6 Gas Insulating HV-Bushing for CRAFT NNBI*

Yu-Chen Qu,^{1,2} Zhi-Min Liu,^{1,2} Cai-Chao Jiang,^{1,2,†} Jiang-Long Wei,¹ Bo Liu,^{1,2} Yuan-Lai Xie,^{1,2} and Xu Wang³

¹*Institute of Plasma Physics, Hefei Institutes of Physical Science, Chinese Academy of Sciences, Hefei 230031, China*

²*University of Science and Technology of China, Hefei 230026, China*

³*China Nuclear Engineering Consulting Co., Ltd., Beijing 100032, China*

The full-scale beam source of CRAFT NNBI is planned to adopt a vacuum-insulated ion source scheme to generate a 400 keV negative hydrogen ion beam through two stages of -200 kV acceleration voltage. A preliminary design has been developed for two stages of -400 kV high-voltage bushings, which are intended for insulating and sealing connections between the SF₆-insulated transmission line and the vacuum chamber. Vacuum-side insulation design has been conducted to analyze and improve the electric field strength of the vacuum-side cathode surface, anode surface, insulator surface, and triple point, meeting the standard requirements specified by the Japan Atomic Energy Agency for high-voltage bushings designed for ITER. The design includes the cooling water flow channels for the -200 kV bushing section, considering the requirements for cooling water flow rate based on the thermal load of the accelerating electrode (AG) and temperature constraints, analyzing pressure drop in the channels and uniformity of flow distribution. Mechanical strength analysis of the bushing structure has been performed, considering the stress and deformation under 0.6 MPa SF₆ gas, 1 MPa air, and gravity loads between the insulating ceramic ring and fiber-reinforced plastic (FRP) ring within the transmission line.

Keywords: NNBI, HV bushing, Vacuum insulation, Cooling water channel, Structural strength

I. INTRODUCTION

The Comprehensive Research Facility for Fusion Reactor Key Technology (CRAFT) is a major scientific infrastructure project under China's "13th Five-Year Plan" for major scientific infrastructure construction. The goal of CRAFT is to establish an internationally leading comprehensive research and testing platform in the field of nuclear fusion, with the highest parameters and most complete functions. One of the components is the Neutral Beam Injection system within the Negative ion source (NNBI) of CRAFT, which is preliminarily planned to achieve a hydrogen neutral beam with an energy of 200 keV-400 keV, power of 2 MW, and pulse width greater than 100 s [1].

Fusion research in tokamak devices necessitates the employment of various auxiliary heating methods to meet the heating and control requirements of the plasma [2]. Neutral Beam Injection (NBI) has demonstrated significant effects in core plasma heating and current drive [3], and is characterized by high heating efficiency and clear physical mechanisms, making it widely used in magnetic confinement fusion devices [4–7]. Advanced fusion experimental devices aimed at future applications [8–10] will target the achievement of fusion ignition conditions and steady-state operation [11], with NBI towards high-energy levels in the MeV range, high power levels in the tens of MW, and quasi-steady-state injection durations in the order of hours [12]. NBI ion sources utilize electrostatic field acceleration, and high-energy beam currents require high-voltage acceleration, thus presenting numerous high-voltage insulation challenges. Hodgson *et*

al.'s research on the insulation gases of the NBI for the International Tokamak Experimental Reactor (ITER) indicated that radiation-induced leakage currents in air and sulfur SF₆ gases would result in unacceptable high power losses [13], leading to the proposal of vacuum-insulated NBI ion source schemes. The ion source is placed within a vacuum chamber, with the required electrical energy, cooling water, and gas supply transmitted from external sulfur SF₆ gas-insulated transmission lines into the vacuum chamber via high-voltage bushings. Numerous studies have been conducted to address the high-voltage insulation issues for ITER NBI [14, 15], and to validate the performance required for ITER NBI, the ITER NBI Test Facility NBTF was constructed in Padua, Italy [16]. M. Boldrin *et al.* discussed design issues related to high-voltage platforms and penetrations [17]. JAEA has designed and manufactured high-voltage components for the DC 1 MV power supply system for NBTF and ITER NBI. This includes a 200 kV first stage with five poles of 1 MV high-voltage bushings, a design scheme that has passed pressure tests [18], thus providing reference for relevant design guidelines. Additionally, there are numerous studies focused on high-voltage insulation for ITER NBI [19, 20], as well as the design work for new types of high-voltage bushings [21].

CRAFT NNBI plans to develop a vacuum insulation scheme and has already initiated research and development work on the negative ion source [22], neutralizer [23] and SF₆ transmission line [24], with the beam source test facility under construction. Design work for sulfur SF₆ transmission lines at even higher voltages is also underway [25], as part of the next phase of development. This paper presents preliminary design work for a -400 kV high-voltage bushing, including: 1. Vacuum insulation design, vacuum-side electrode, insulator, and cathode three-phase point electric field analysis. 2. High-speed cooling water channel design, pressure drop of cooling water flow and flow distribution in multiple parallel channels. 3. Mechanical structure design, considering the pressure of insulating gas and gravitational loads, analyzing

* Supported by the National Natural Science Foundation of China (11975263), (11975264); National Major Science and Technology Infrastructure Project of China(2018-000052-73-01-001228)

† Corresponding author, jcch@ipp.ac.cn

the magnitude of structural stress and mechanical deformation.

II. OVERALL DESIGN OF HV BUSHINGS

The structure of the HV bushings is shown in Fig. 1, consisting of two levels of bushings at -400 kV and -200 kV coaxially nested together. The bushings' electrostatic screens are fixed to the flanges, with ceramic rings and fiber-reinforced plastic rings (FRP) coaxially positioned between the flanges to provide insulation, support, and sealing. The inner side of the bushings is under vacuum, while the outer side is connected to the SF6 transmission line, filled with SF6 insulation gas at a pressure of 0.6 MPa. Dry air at a pressure greater than 0.6 MPa is present between the ceramic rings and fiber-reinforced plastic rings to prevent SF6 gas leakage into the vacuum. The ceramic rings are brazed sealed to Kovar rings, while the fiber-reinforced plastic rings and Kovar rings are sealed to the bushings flanges using sealing rings in a compression manner. The structure simplification ignores the structure of the SF6 transmission line section and the cooling water flow channel section of the -200 kV bushings.

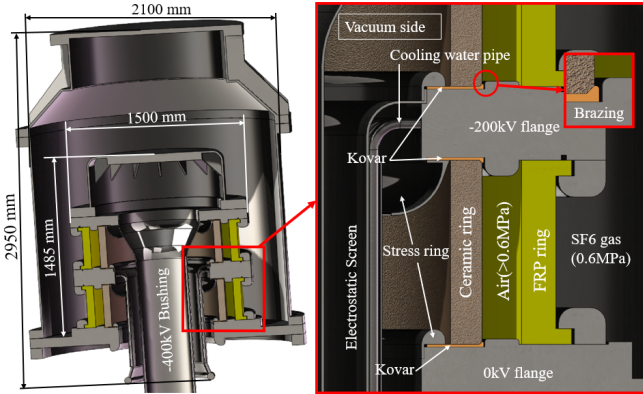


Fig. 1. Cross sectional view of CRAFT NNBI HV bushing.

The CRAFT NNBI ion source has been designed in previous work, Fig. 2 shows the power supply structure and estimated power load of the accelerator section [24]. The accelerator is divided into four layers. The ground grid (GG) is at the same potential as the vacuum chamber wall. The acceleration grid (AG) is connected to the -200 kV bushings for power supply. The inner diameter of the -200 kV electrostatic screen is 295 mm, and the outer diameter is 325 mm. The bottom of the electrostatic screen expands and is equipped with a pressure equalization ring to reduce the electric field intensity. The outer diameter of the pressure equalization ring is smaller than the inner diameter of the 0 kV flange for ease of engineering assembly. Due to space limitations, compact high-speed cooling water flow channels need to be designed to dissipate the 500 kW heat load from the AG, as shown in Fig. 3. The six parallel pipelines on the electrostatic screen form a set of flow channels, intersecting inside the flange and at the bottom of the pressure equalization ring. There are a

total of four sets of cooling water flow channels, with two sets each flowing in and out of the AG. Additional shielding housings are installed on the external of the pipelines on the electrostatic screen to shield the electric field and prevent field concentration near the pipelines, reducing insulation performance. The extraction grid (EG) is connected to the -400 kV bushings for power supply. The power supply for the plasma grid (PG), RF plasma source, EG cooling water pipelines, etc., are all located inside the outer diameter of the -400 kV bushings, which is 430 mm. The lower end of the electrostatic screen is directly connected to the plasma source of the accelerator, thus eliminating the need for a pressure equalization ring.

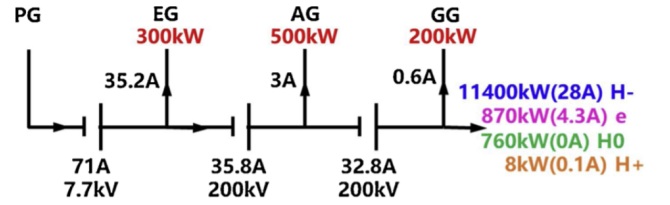


Fig. 2. Accelerator power supply and power estimation.

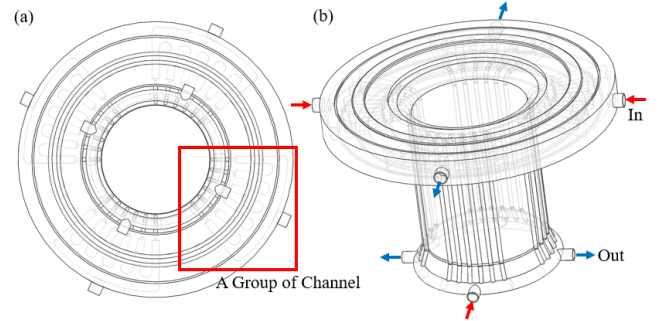


Fig. 3. -200 kV screen cooling water channel. bottom view (a), oblique view (b).

III. VACUUM INSULATION

A. Design standards

The HV bushing has two insulation clearances to maintain a 400 kV voltage. H. Tobari. *et al* experimentally studied the voltage maintenance capability of HV bushings with multiple clearances and provided an empirical formula for voltage maintenance capability [26],

$$(EV)^{0.5} = \frac{V}{(r_c \ln(r_a/r_c))^{0.5}} > k^{0.5} = 36S6-0.18 \quad (1)$$

Where $E(kV/mm)$ is the electric field strength on the cathode surface and $V(kV)$ is the gap maintenance voltage. Considering the HV bushing as a coaxial electrode, the electric

field on the cathode surface is calculated by the outer electrode radius, r_a , and the inner electrode radius, r_c . According to the Clump theory [27], breakdown occurs when the product of the charge Q and the voltage V exceeds a certain threshold. Since Q is proportional to the electric field strength on the electrode surface, the product of Q and V is converted into the product of E and V , with a corresponding threshold value, k , related to the sum of the cathode total area, $S(m^2)$.

During the early research on the single gap-single aperture (SINGAP) beam source [28–30], A. Masiello proposed key electric field constraints for the design standards of high-voltage bushing vacuum insulation [31], and compared them with another set of design standards, as seen in Tab. 1. The Japan Atomic Energy Agency (JAEA) referenced these standards in the design of the ITER NNBI high-voltage bushing [32], but the electric field at the cathode triple point did not meet the standard limits. JAEA conducted high-voltage hold tests to verify the reliability of the limits provided by these design standards [19], demonstrating their validity. However, in the high-voltage bushing designed for NBTF, a safety margin was taken into account, adopting a cathode surface electric field limit standard of 3 kV/mm. Note that the amplitude of the surface electric field refers to the region near the surface, not on the surface itself. The strictly defined surface electric field amplitude is the average of the electric field amplitudes near both sides of the surface. The surface electric fields mentioned in this paper refer to the electric fields in the vicinity of the surface.

B. Bushing design

The main design parameters of the CRAFT NNBI HV bushing are shown in Tab. 2. The values for electric field limitations were comprehensively determined based on relevant experimental results and design standards. Considering the dimensions of internal pipes and cables, the diameter of the -400 kV electrostatic shield was first determined, followed by calculating the dimensions of other electrostatic shields based on the electric field limitations. The voltage maintenance capability for each gap was calculated using empirical Eq. 1. The cathode area for the -400 kV to -200 kV gap is $1.89 m^2$, with a voltage maintenance capability of 238 kV. For the -200 kV to 0 kV gap, the cathode area is $1.52 m^2$, with a voltage maintenance capability of 263 kV, meeting the design requirements. While ensuring insulation capability, it is desired to minimize the overall size of the bushing as much as possible. This can reduce costs, especially since larger ceramic insulating rings are more expensive, and the brazing technology for ceramic rings and Kovar rings is limited by size. Additionally, smaller size implies greater structural strength and vacuum maintenance reliability. Based on the dimensions of the main components, a COMSOL software analysis was conducted to adjust the geometric shape of a 2D axisymmetric model for electric field analysis, resulting in a structural model with electric field amplitudes that meet design standards, as shown in Fig. 4. The maximum electric field value on the cathode surface of the electrostatic shield

is approximately 2.9 kV/mm. The electric field on the anode surface increases at stress rings and other bending points, but the electric field amplitudes at all locations are below the limit. The function of the stress ring (shown in Fig. 1) is similar to a pressure ring, but its main purpose is to reduce the electric field amplitude at the triple point. According to the standard in Tab. 1, the electric field amplitude at the cathode triple point should be less than 0.1 kV/mm to prevent surface flashover. This is a very stringent limitation, so an asymmetric stress ring design was implemented, with a larger cathode stress ring and a smaller anode stress ring, while both gaps have the same stress ring size. However, the electric field amplitude at the cathode triple point does not meet the design standard.

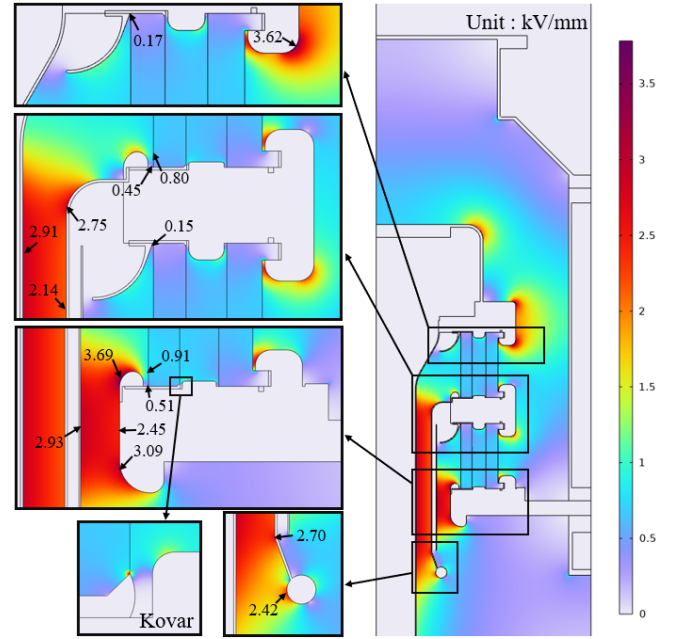


Fig. 4. Electric field amplitude for a 2D analysis.

Increasing the size of the stress ring further does not effectively reduce the electric field amplitude at the triple point. Increasing the diameter of the stress ring to bring it closer to the ceramic insulating ring can lower the electric field amplitude, but the distance between them cannot be too close, considering manufacturing precision, and is set 2 mm. Additionally, adding a raised metal ring on the flange between the ceramic ring and the FRP ring can reduce the electric field amplitude at the triple point, but it also increases the electric field amplitude on the surface of the ceramic insulating ring facing the vacuum side. Ultimately, it was decided to have a 3 cm high metal ring on the cathode and a 1 cm high metal ring on the anode. The electric field amplitude at the cathode triple point for the -400 kV flange is 0.17 kV/mm, and for the -200 kV flange is 0.15 kV/mm, which does not meet the design standard but satisfies the DDD 5.3 standard. Improvements in the surface roughness, geometric configuration, and temperature parameters of the insulating ring can further suppress the occurrence of surface flashover [33].

TABLE 1. Design criteria for vacuum electric field in the HV bushing.

Position	Electric field limits (kV/mm)	DDD5.3 limit (kV/mm)
Cathode surface (200 kV)	< 4	< 10
Cathode surface (1000 kV)	< 3	—
Insulator surface	< 1	—
Cathode triple point	< 0.1	< 1

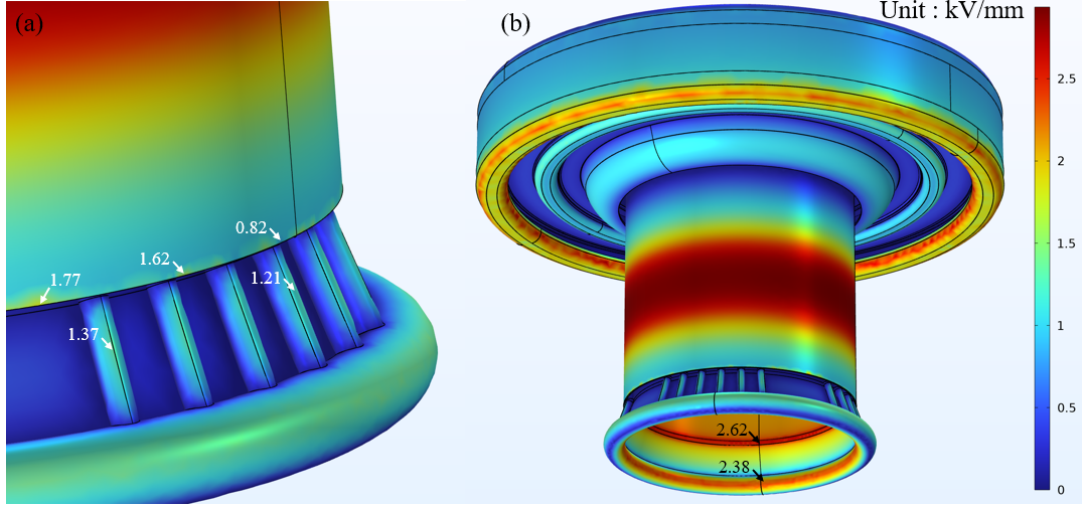
Fig. 5. -200 kV electrostatic screen electric field amplitude for a 3D analysis. around cooling water pipes (a), screen overall (b).

TABLE 2. Main design parameters of CRAFT NNBI HV bushing.

Parameter	Value
Cathode surface electric field	< 3 kV/mm
Other electrode surface electric field	< 4 kV/mm
Insulator surface	< 1 kV/mm
Cathode triple point	< 0.17 kV/mm
-400 kV screen diameter	430 mm
-400 kV ~ -200 kV gap length	80 mm
-200 kV screen diameter	650 mm
-200 kV ~ 0 kV gap length	75 mm
Flange diameter	1500 mm
Ceramic ring diameter	1030 mm
FRP ring diameter	1310 mm

The cathode triple point electric field in the HV bushing design for ITER NNBI did not meet the design standard, but its reliability was verified through high-voltage maintenance tests. The cathode triple point electric field amplitude in the CRAFT NNBI bushing design is lower than that of ITER NNBI. During the brazing of ceramic and Kovar rings, there may be overflow of brazing material forming irregular boundaries. Therefore, the design includes embedding the Kovar ring into the flange to a certain depth, with the brazing area shielded by the metal ring on the flange to have a very low electric field amplitude, avoiding irregular boundaries of brazing material enhancing the electric field beyond design limits.

The analysis of the 2D axisymmetric electric field cannot calculate the electric field near the cooling water pipes on the

-200 kV electrostatic screen. In order to ensure the reliability of the insulation design, a 3D electric field analysis of the -200 kV electrostatic screen was conducted, and the results are shown in Fig. 5. The electric field near the cooling water pipes is non-uniform, with the maximum electric field magnitude appearing at the edge of each group of cooling water pipes being 1.37 kV/mm. Non-uniform electric fields also appear at the edges of the shielding shell of the pipes, and the distribution pattern is influenced by the arrangement of the pipes. The electric field magnitude obtained from the three-dimensional analysis is slightly smaller than that from the two-dimensional analysis, and finite element analysis is limited by the grid size, which may cause distortion of the electric field in small structures. However, the electric field magnitudes in all areas are far below the standard limits.

IV. COOLING WATER CHANNEL

When the CRAFT NNBI ion source operates at full power, it is expected to generate a heat load of 500 kW on the AG due to the bombardment of charged particles. In order to meet the requirements of long-pulse operation, an equally powerful cooling capacity is needed, thus a high-speed cooling water flow channel is designed. Under normal operating conditions, the cooling water temperature can rise to over 30°C during steady-state operation of the accelerator, corresponding to a mass flow rate of approximately 4 kg/s. However, for the design of the accelerator, it is desired to minimize the deformation of the electrodes caused by temperature changes in order

to achieve more stable accelerator performance. According to calculations based on a 6°C temperature rise of the cooling water [34], the mass flow rate of the cooling water is approximately 20 kg/s. The four sets of channels are divided into two inlet and two outlet groups, with each group of channels carrying half of the total flow rate. Using the Fluent software $k-\omega$ model, the flow analysis in the AG direction for a set of channels with mass flow rates ranging from 2 to 10 kg/s for both inflow and outflow was conducted.

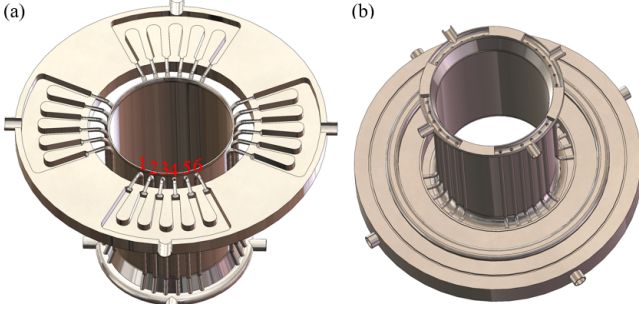


Fig. 6. Cross sectional view of cooling water channel. Inside the flange (a), Inside the grading ring (b).

The cross-sectional views of the cooling water flow channels in the electrostatic screen and flange are shown in Fig. 6, illustrating the internal structures of the upper flange and the bottom equal pressure ring of the flow channels. The cross-sectional area of the above two parts of the channels is much larger than that of the six parallel pipes, concentrating the pressure gradient at the entrance of the pipes, which can suppress flow instability in the parallel channels and help balance the flow distribution. Fig. 7 shows the pressure distribution inside the channels when the mass flow rate is 6 kg/s, with significant pressure drops at the entrances of the six parallel pipes for both inflow and outflow, accounting for approximately 50% and 60% of the total pressure drop, respectively, without flow instability between the parallel pipes observed in the simulation. The pressure drop variations in the channels are shown in Fig. 8, with the pressure drop in the inflow direction of the AG being lower than that in the outflow direction. At maximum flow rate, the inlet pressure drop is 109.9 kPa, while the outlet pressure drop is 117.1 kPa, a difference of 6.5%. The flow distribution within the parallel pipes is shown in Fig. 9, with better uniformity in the inflow direction of the AG compared to the outflow direction. At a mass flow rate of 8 kg/s, the deviation in flow distribution is greatest, with forward flow deviation at 8.3% and reverse flow deviation at 11.5%. Since the inlet and outlet of the channels are positioned at the center of pipes 3 and 4, these two pipes have higher flow rates in all cases, and the distribution uniformity does not follow a consistent pattern with flow rate. The performance of the inflow direction of the AG is better than that of the outflow direction, as the cross-sectional area of the channels within the equal pressure ring is smaller, resulting in higher turbulence intensity when the cooling water exits the AG and is distributed to the six pipes within the equal pressure ring, dissipating more energy and leading to greater pressure

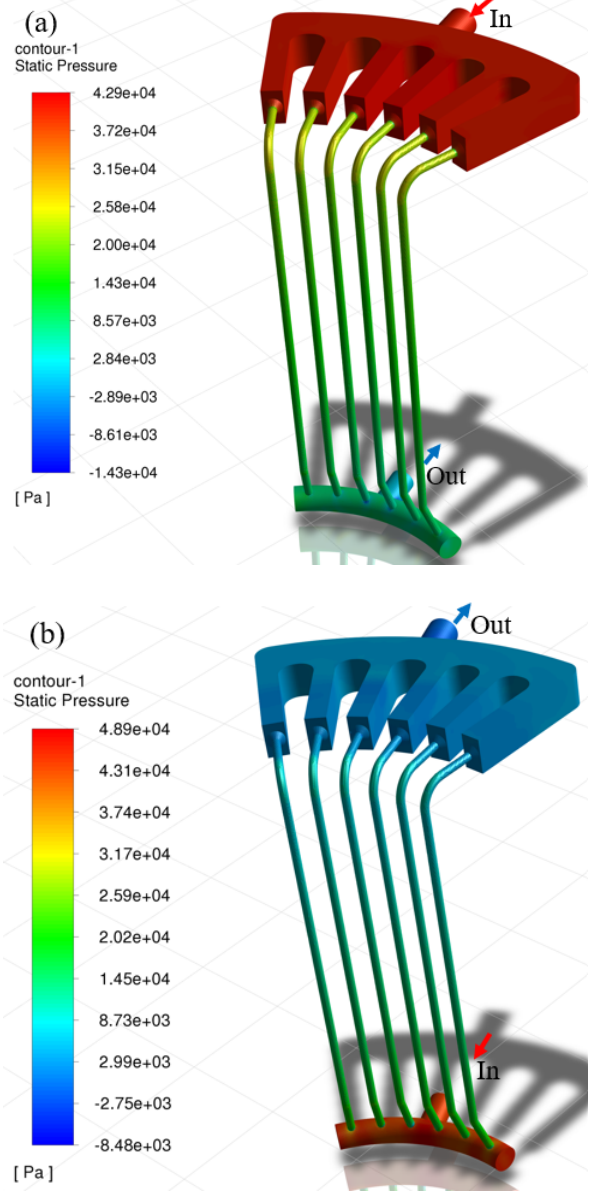


Fig. 7. The pressure distribution in the channel with a 6 kg/s mass flow rate. Cooling water flows into the AG direction (a), Cooling water flows out of AG direction (b).

drop, as well as a more chaotic flow field and poorer flow distribution uniformity. Through analysis, it is concluded that the performance of the channels is acceptable and can meet the cooling water supply requirements.

V. STRUCTURAL STRENGTH

The HV bushing is connected to the SF6 transmission line on one side, subjected to a pressure of 0.6 MPa of SF6 gas, and connected to an ion source in a vacuum on the other side. Dry air pressure between the ceramic ring and the FRP ring may reach up to 1 MPa. A comprehensive structural strength

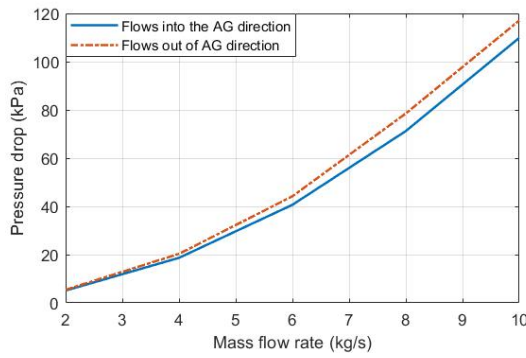


Fig. 8. The relationship between pressure drop and flow rate in the channel.

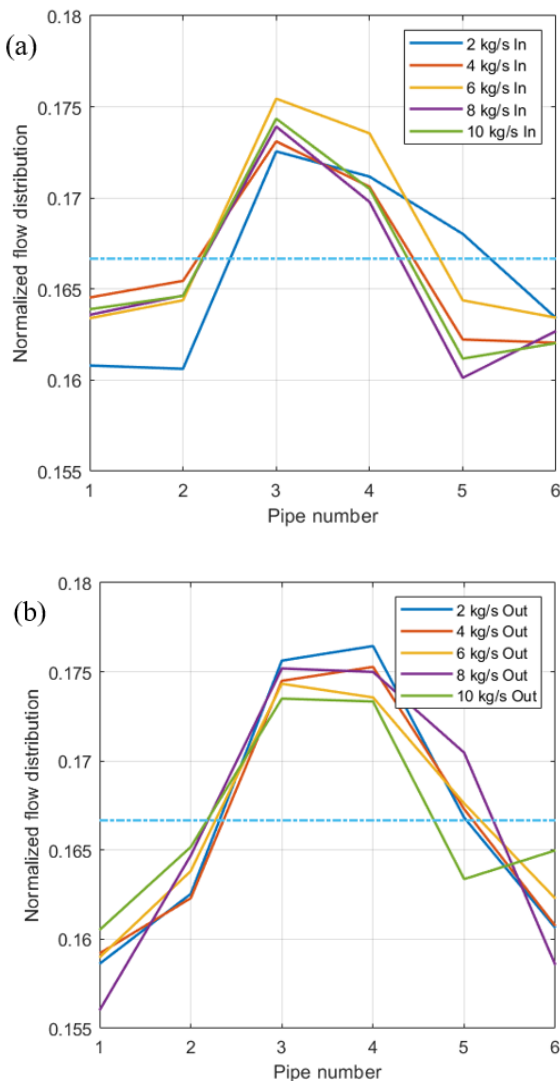


Fig. 9. Flow distribution in parallel pipelines. Cooling water flows into the AG direction (a), Cooling water flows out of AG direction (b).

analysis is conducted considering the gas pressure and the

gravitational effects on the bushing. The physical properties of the materials are shown in Tab. 3. The mechanical properties are referenced in Tab. 4, including the tensile strength of the ceramic and Kovar brazed joint as provided by H. Tobari *et al.* [35], as well as the mechanical properties of two types of FRP materials. The tensile strength at the brazed joint is based on the average value from a specific tensile test, but with a relatively large dispersion. Previously, P. Zaccaria *et al.* [36] established a fault probability assessment procedure for the brazing process of ceramic rings and metal plates, conducting a thermomechanical and failure probability analysis of the ceramic insulator rings during the brazing process. The Von-Mises stress distribution of the overall structure of the HV bushing is shown in Fig. 10, with the maximum stress point located on the reinforcement rib of the -400 kV electrostatic screen cover. The maximum stress of 88.4 MPa is significantly lower than the tensile strength of stainless steel material. The deformation distribution is shown in Fig. 11, with the maximum deformation of 0.545 mm occurring at the cover position, which is not significant as it will be connected to the -400 kV transmission line. The overall downward deformation of all electrostatic screens is approximately 0.236 mm, mainly caused by the deformation of the 0 kV flange under the pressure of SF₆ gas, resulting in a relatively small relative deformation of 0.013 mm between the two electrostatic screens, which cannot be neglected in terms of its impact on the electric field distribution.

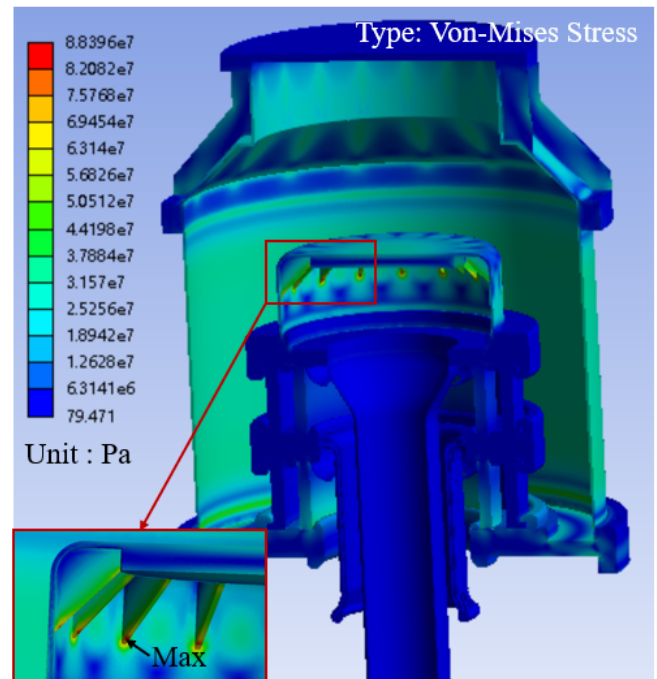


Fig. 10. Von-Mises stress of HV-bushing.

The maximum stress near the brazed area on the ceramic ring reaches 24.6 MPa, appearing at the base end of the ceramic ring between 0 kV and -200 kV as shown in Fig. 12. This stress is mainly caused by the deformation of the 0 kV flange. Designing reinforcement ribs on the 0 kV flange can

TABLE 3. Physical properties of materials.

Material	Elasticity modulus (GPa)	Poisson ratio	Density(kg/m ³)
Stainless steel	197	0.29	7930
Kovar	130	0.37	7850
Alumina ceramic	343	0.25	3800
FRP	20	0.3	2200

TABLE 4. Mechanical properties of materials.

Material	Tensile strength (MPa)	Compressive strength(MPa)	Shear strength (MPa)
Filament winding FRP	130	110	25
Fiber cloth FRP	327	279	56
Brazing	103±40	—	—
Stainless steel	460	250	—

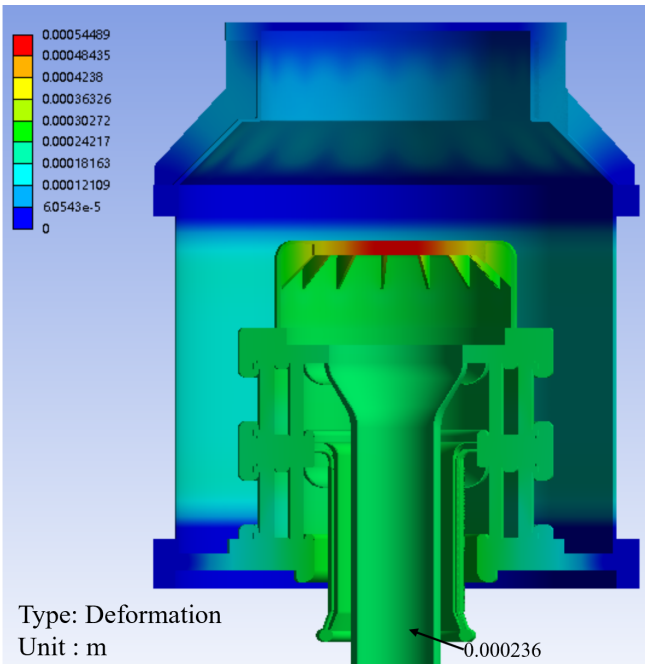


Fig. 11. Deformation of HV-bushing.

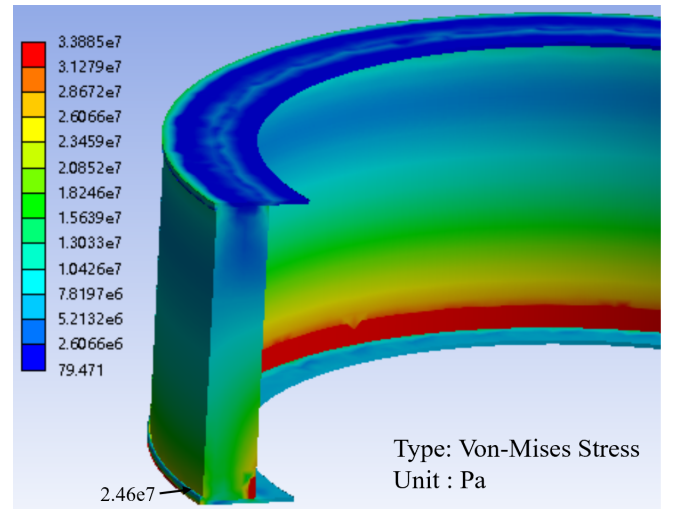


Fig. 12. Von-Mises stress of 0 kV ~ -200 kV ceramic ring.

reduce the stress on the ceramic ring and the overall structural deformation. The maximum stress on the FRP ring is 6.62 MPa, and the maximum shear stress is 3.81 MPa, also occurring on the FRP ring between 0 kV and -200 kV as shown in Fig. 13. The strength of both manufacturing processes for the FRP meets the requirements.

VI. SUMMARY

The CRAFT NNBI HV bushing is used to connect the SF₆ gas transmission line and the vacuum-insulated ion source for the transmission of electrical energy, gas, and cooling water. Preliminary designs were conducted for vacuum insulation, cooling water channels, and structural strength. The results are as follows:

1. The high voltage withstand capability of the vacuum insulation was calculated using empirical formulas, meeting the voltage requirements. The electric field restriction standards for vacuum insulation were determined, and electric field analysis was performed. The maximum electric field intensity on the cathode surface was 2.93 kV/mm, on the anode surface was 3.69 kV/mm, and on the ceramic insulating ring surface was 0.91 kV/mm, all meeting the standards. The electric field at the vacuum cathode triode point reached 0.17 kV/mm, which did not meet the limiting value. However, based on JAEA's experimental tests, the design of the cathode triode point electric field exceeding the standard limit still meets the insulation requirements.
2. The cooling water channel on the -200 kV bushing was designed. Considering the heat load and temperature changes on the AG, the required cooling water flow rate range of 2 to 10 kg/s was determined. A cooling water channel design consisting of six parallel pipes as a group was developed, considering the suppression of unstable flow in parallel channels, with good results. Analysis of pressure drops in the forward and reverse flow of the channels and the flow distribution in parallel pipes was conducted. The maximum pressure drop

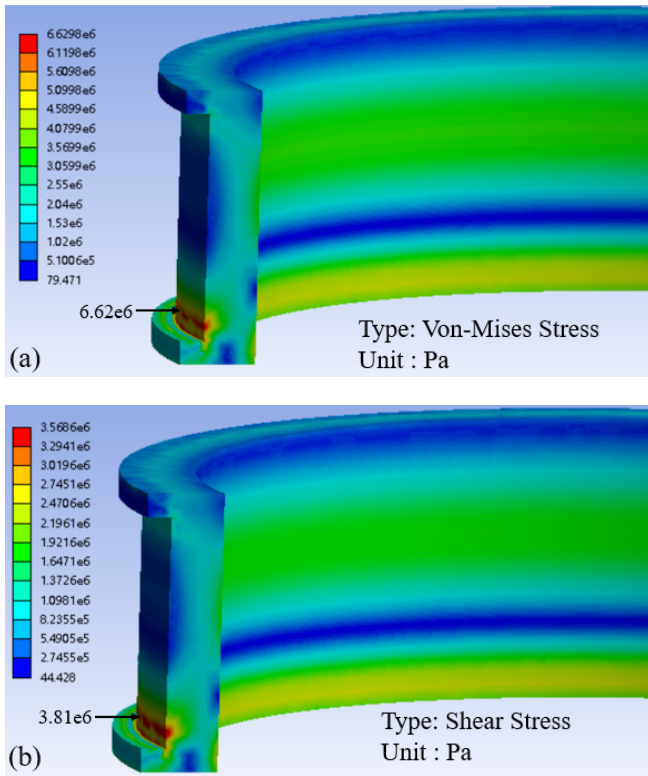


Fig. 13. stress of 0 kV ~ -200 kV FRP ring. Von-Mises stress (a), Shear stress (b).

in the channels did not exceed 120 kPa, within an acceptable range. The flow distribution deviation between parallel pipes was a maximum of 8.3% in the forward direction and 11.5% in the reverse direction.

3. Overall structural strength analysis was conducted, considering the pressure loads of 0.6 MPa SF₆ gas and 1 MPa air, as well as the self-weight loads. The maximum Von-Mises stress on the stainless steel structure was 88.4 MPa, with the maximum Von-Mises stress near the brazed area of the ceramic insulating ring being 24.6 MPa, and the maximum Von-Mises stress and shear stress on the FRP ring being 6.62 MPa and 3.81 MPa, respectively. The stresses on each component were significantly lower than the material strength, providing sufficient safety margin. The overall deformation of the bushing was 0.236 mm, with a relative deformation of 0.013 mm between the electrostatic screens, which would not significantly affect the electric field distribution.

VII. ACKNOWLEDGEMENTS

This work was supported by the National Natural Science Foundation of China (No.11975263), (No.11975264) and the Comprehensive Research Facility for Fusion Technology Program of China (No.2018-000052-73-01-001228).

- [1] Q.L. Cui, J.L. Wei, Y.H. Xie, et al., Beamlet optics analysis of 400 keV accelerator for CRAFT negative ion based neutral beam injection system. *High Power Laser and Particle Beams* **35**(11), 74-80 (2023). doi: [10.11884/HPLPB202335.230179](https://doi.org/10.11884/HPLPB202335.230179)
- [2] M.J. Singh, D. Boilson, R. Hemsworth, et al., Heating neutral beams for ITER: Present status. *IEEE 26th Symposium on Fusion Eng.* 1-6 (2015). doi: [10.1109/SOFE.2015.7482422](https://doi.org/10.1109/SOFE.2015.7482422)
- [3] E. Speth, Neutral beam heating of fusion plasmas. *Rep. Prog. Phys.* **52**(1), 57 (1989). doi: [10.1088/0034-4885/52/1/002](https://doi.org/10.1088/0034-4885/52/1/002)
- [4] A.F. Lifschitz, A. Revel, L. Caillault, et al., Numerical study of beam propagation and plasma properties in the neutralizer and the E-RID of the ITER Neutral Beam Injector. *Nucl. Fusion* **54**(4), 043020 (2014). doi: [10.1088/0029-5515/54/4/043020](https://doi.org/10.1088/0029-5515/54/4/043020)
- [5] M.X. Chen, C.Y. Liu, S.B. Shu, et al., Simulation of EAST current drive by neutral beam injection. *Journal of Hefei University of Technology* **38**(12), 1716-1719 (2015). doi: [10.3969/j.issn.1003-5060.2015.12.026](https://doi.org/10.3969/j.issn.1003-5060.2015.12.026)
- [6] T.L. Zhang, K.Y. Jiang, Z.W. Liu, et al., Characteristics of inductively coupled plasma (ICP) and helicon plasma in a single-loop antenna. *Plasma Sci. Technol.* **22**(8), 085405 (2020). doi: [10.1088/2058-6272/ab8551](https://doi.org/10.1088/2058-6272/ab8551)
- [7] P. Vincenzi, J.F. Artaud, E. Fable, et al., Neutral beam injection for DEMO alternative scenarios. *Fusion Eng. Des.* **163**, 112119 (2021). doi: [10.1016/j.fusengdes.2020.112119](https://doi.org/10.1016/j.fusengdes.2020.112119)
- [8] V. Toigo, R. Piovan, S.D. Bello, et al., The PRIMA Test Facility: SPIDER and MITICA test-beds for ITER neutral beam injectors. *New J. Phys.* **19**(8), 085004 (2017). doi: [10.1088/1367-2630/aa78e8](https://doi.org/10.1088/1367-2630/aa78e8)
- [9] P. Sonato, P. Agostinetti, T. Bolzonella, et al., Conceptual design of the DEMO neutral beam injectors: main developments and R&D achievements. *Nucl. Fusion* **57**(5), 056026 (2017). doi: [10.1088/1741-4326/aa6186](https://doi.org/10.1088/1741-4326/aa6186)
- [10] Y.X. Wan, J.G. Li, Y. Liu, et al., Overview of the present progress and activities on the CFETR. *Nucl. Fusion* **57**(10), 102009 (2017). doi: [10.1088/1741-4326/aa686a](https://doi.org/10.1088/1741-4326/aa686a)
- [11] C.D. Hu, L.Z. Liang, Y.L. Xie, et al., Conceptual design of neutral beam injection system for CFETR. *Nucl. Fusion Plasma Phys.* **42**(4), 388-392 (2022). doi: [10.16568/j.0254-6086.202204005](https://doi.org/10.16568/j.0254-6086.202204005)
- [12] Y.H. Xie, C.D. Hu, J.L. Wei, et al., Conceptual design of negative ion based beam source for CFETR neutral beam injector. *Nucl. Fusion Plasma Phys.* **41**(4), 628-634 (2021). doi: [10.16568/j.0254-6086.202104008](https://doi.org/10.16568/j.0254-6086.202104008)
- [13] E.R. Hodgson, A. Morono, Radiation effects on insulating gases for the ITER NBI system. *J. Nucl. Mater.* **258-263**, 1827-1830(1998). doi: [10.1016/S0022-3115\(98\)00345-6](https://doi.org/10.1016/S0022-3115(98)00345-6)
- [14] M. Tanaka, R. Hemsworth, M. Kuriyama, et al., 1 MW Vacuum insulation for the ITER neutral beam injectors. 24th IS-DEIV 536-539 (2010). doi: [10.1109/DEIV.2010.5625756](https://doi.org/10.1109/DEIV.2010.5625756)
- [15] E.D. Pietro, T. Amemiya, M. Hanada, et al., Design and overview of fabrication tests for the 1 MV bushing for ITER NB system. *Fusion Eng. Des.* **49**(5), 055022(2009). doi: [10.1088/0029-5515/49/5/055022](https://doi.org/10.1088/0029-5515/49/5/055022)
- [16] H. Tobari, M. Kashiwagi, K. Watanabe, et al., Progress on design and manufacturing of dc ultra-high voltage component for ITER NBI. *Fusion Eng. Des.* **123**, 309-312 (2017). doi: [10.1016/j.fusengdes.2017.05.001](https://doi.org/10.1016/j.fusengdes.2017.05.001)

- 10.1016/j.fusengdes.2017.05.017
- [17] M. Boldrin, M.D. Palma, F. Milani, et al., Design issues of the High Voltage platform and feedthrough for the ITER NBI Ion Source. *Fusion Eng. Des.* **84**(2-6), 470-474 (2008). doi: 10.1016/j.fusengdes.2008.11.013
- [18] H. Tobari, M. Taniguchi, M. Kashiwagi, et al., Vacuum Insulation and Achievement of 980 keV, 185 A/m² H⁻ Ion Beam Acceleration at JAEA for the ITER Neutral Beam Injector. *Plasma Sci. Technol.* **15**(2), 179-183 (2013). doi: 10.1088/1009-0630/15/2/21
- [19] A. Delorenzi, N. Pilan, G. Chitarin, et al., HV Holding in Vacuum, a Key Issue for the ITER Neutral Beam Injector. 28th ISDEIV 721-730 (2018). doi: 10.1109/DEIV.2018.8537143
- [20] K. Watanabe, M. Yamamoto, J. Takemoto, et al., Design of a -1 MV dc UHV power supply for ITER NBI. *Nucl. Fusion* **49**(5), 055022 (2009). doi: 10.1088/0029-5515/49/5/055022
- [21] A. Simonin, H.de Esch, L. Doceul, et al., Conceptual design of a high-voltage compact bushing for application to future N-NBI systems of fusion reactors. *Fusion Eng. Des.* **88**(1), 1-7 (2013). doi: 10.1016/j.fusengdes.2012.04.025
- [22] Y.H. Xie, C.D. Hu, J.L. Wei, et al., Conceptual design of a beam source for negative neutral beam injector of CRAFT facility. *Fusion Eng. Des.* **167**, 112377 (2021). doi: 10.1016/j.fusengdes.2021.112377
- [23] J.L. Wei, Z.Y. Zhang, W. Yi, et al., Thermo-mechanical design of the neutralizer for CRAFT negative ion-based neutral beam injection system. *Fusion Eng. Des.* **169**, 112482 (2021). doi: 10.1016/j.fusengdes.2021.112482
- [24] R.X. Wang, C.C. Jiang, Y.J. Xu, et al., Electrostatic analysis and preliminary design of transmission line for the CRAFT NNBI test platform. *Fusion Eng. Des.* **165**, 112259 (2021). doi: 10.1016/j.fusengdes.2021.112259
- [25] B. Liu, Z.M. Liu, C.C. Jiang, et al., Insulation design of -800 kV gas insulation transmission line for negative ion based neutral beam injector. *Fusion Eng. Des.* **196**, 114027 (2023). doi: 10.1016/j.fusengdes.2023.114027
- [26] H. Tobari, K. Watanabe, M. Kashiwagi, et al., DC Ultrahigh Voltage Insulation Technology for 1 MV Power Supply System for Fusion Application. *IEEE T. Plasma Sci.* **45**(1), 162-169 (2001). doi: 10.1109/TPS.2016.2632762
- [27] L. Cranberg, The Initiation of Electrical Breakdown in Vacuum. *J. Appl. Phys.* **23**(5), 518-522 (1952). doi: 10.1063/1.1702243
- [28] P. Massmann, P. Bayetti, J. Bucalossi, et al., European contributions to the beam source design and R&D of the ITER neutral beam injectors. *Nucl. Fusion* **40**(3Y), 589-597 (2000). doi: 10.1088/0029-5515/40/3Y/321
- [29] J. Bucalossi, C. Desgranges, R.S. Hemsworth, et al., Beam Optics of the SINGAP 1 MeV 100 mA D⁻ DC Accelerator for Thermonuclear Fusion. *Rev. Sci. Instrum.* **70**, 1991-1993 (1999). doi: 10.1063/1.1149700
- [30] P. Massmann, D. Boilson, H.de Esch, R.S. Hemsworth, et al., Voltage holding and dark currents in the Cadarache 1 MV ion beam facility. 20th ISDEIV 315-318 (2002). doi: 10.1109/IS-DEIV.2002.1027372
- [31] A. Masiello, Adaptation of the 1 MV bushing to the SINGAP concept for the ITER NB injector test bed. *Nucl. Fusion* **46**(6), S340-S351 (2006). doi: 10.1088/0029-5515/46/6/S16
- [32] N. Umeda, M. Taniguchi, M. Kashiwagi, et al., Development of 1 MV accelerator and HV bushing at JAEA toward ITER Neutral Beam system. *Fusion Eng. Des.* **84**(7), 1875-1880 (2009). doi: 10.1016/j.fusengdes.2008.12.018
- [33] G.Y. Sun, B.P. Song, B.H. Gou, et al., Estimation of surface flashover threshold in vacuum: from multipactor to discharge plasma. *J. Phys. D: Appl. Phys.* **51**(29), 295201 (2018). doi: 10.1088/1361-6463/aacccf
- [34] J.L. Wei, C.D. Hu, Y.H. Xie, et al., Physics and engineering design of 400 keV H⁻ accelerator for negative ion based neutral beam injection system in China. *Rev. Sci. Instrum.* **90**(11), 113313 (2019). doi: 113313. DOI:10.1063/1.5128335
- [35] H. Tobari, T. Inoue, M. Taniguchi, et al., Structural analyses of HV bushing for ITER heating NB system. *Fusion Eng. Des.* **88**(6), 975-979 (2001). doi: 10.1016/j.fusengdes.2013.02.020
- [36] P. Zaccaria, S.D. Bello, N. Pilan, Thermo-mechanical analyses of large ceramic rings during brazing process. *Fusion Eng. Des.* **82**, 2588-2594 (2007). doi: 10.1016/j.fusengdes.2007.05.075